

# Superconductivity in twisted WSe<sub>2</sub> from topology-induced quantum fluctuations

Fang Xie,<sup>1,2,\*</sup> Lei Chen,<sup>1</sup> Shouvik Sur,<sup>1</sup> Yuan Fang,<sup>1</sup> Jennifer Cano,<sup>3,4,†</sup> and Qimiao Si<sup>1,‡</sup>

<sup>1</sup>*Department of Physics & Astronomy, Extreme Quantum Materials Alliance,  
Smalley-Curl Institute, Rice University, Houston, Texas 77005, USA*

<sup>2</sup>*Rice Academy of Fellows, Rice University, Houston, Texas 77005, USA*

<sup>3</sup>*Department of Physics and Astronomy, Stony Brook University, Stony Brook, NY 11794, USA*

<sup>4</sup>*Center for Computational Quantum Physics, Flatiron Institute, New York, NY 10010, USA*

(Dated: August 20, 2024)

Recently, superconductivity has been observed in twisted WSe<sub>2</sub> moiré structures (Xia et al., arXiv:2405.14784; Guo et al., arXiv:2406.03418). Its transition temperature is high, reaching a few percent of the Fermi temperature scale. Here, we advance a mechanism for superconductivity based on the notion that electronic topology enables quantum fluctuations in a suitable regime of intermediate correlations. In this regime, the Coulomb interaction requires that an active topological flat band and nearby wider bands are considered together. Compact molecular orbitals arise, which experience quantum fluctuations through topology-dictated hybridization with the other molecular orbitals. The hybridization competes with the active flat band's natural tendency towards static electronic ordering, thereby weakening the latter; we link this effect with certain salient observations by experiments. Furthermore, the competition yields a quantum critical regime where quasiparticles are lost. The corresponding quantum critical fluctuations drive superconductivity. Broader implications and new connections among correlated materials platforms are discussed.

*Introduction* Moiré materials represent a rich platform to realize a plethora of strong correlation phenomena, spanning over Chern insulators, strange metals and superconductors [1–11]. In these materials, exemplified by twisted bilayer graphene and transition metal dichalcogenides (TMDCs), both band topology and electronic correlations play key roles in organizing the phase diagram. These features, in combination with the high tunability of the moiré potential and carrier concentration, have led to a practical platform for not only realizing phenomena reminiscent of other classes of strongly correlated systems, such as heavy fermion compounds and cuprates [12, 13], but also accessing novel types of emergent behaviors [14].

Although superconductivity was identified early on in twisted bilayer graphene, only very recently has it been observed in any moiré TMDCs [15, 16]. Interestingly, the superconducting state in these twisted homo-bilayer WSe<sub>2</sub> (tWSe<sub>2</sub>) systems is realized close to half-band filling. It is characterized by a critical temperature  $T_c$  of a few percent of  $T_F$ , the Fermi temperature, and a coherence length  $\xi \sim 10a_M$  with  $a_M$  being the moiré lattice constant. Both features are similar to that of typical superconducting states realized in correlated systems such as high- $T_c$  cuprates and heavy fermion compounds, and indicative of a strong pairing regime [17–19]. Moreover, depending on the twist angle, the superconducting state was observed to lie in the vicinity of a correlated phase [15, 16]. For a flat band whose partial filling is commensurate, realizing a non-superconducting correlated state is not too surprising. What is striking is that

tuning non-thermal parameters such as the displacement field can readily suppress this state in favor of the superconductor. The latter also provides strong evidence for the unconventional nature of superconductivity. In contrast, in moiré graphene systems, it is still a subject of debate as to whether the observed superconductivity is unconventional [20–23].

Continuum models with parameters fitted to density functional theory calculations indicate that the bandwidth of the active bands in tWSe<sub>2</sub> is greatly suppressed by the moiré potential [24–26]. The presence of such a flat band within the active-band subspace, together with a Coulomb interaction strength that is expected to be larger than both the width of the flat band and its gap to wider bands (see below), guide our consideration. Because of these two features, we study the problem by analogy with the approach we have advanced for the active flat and wide bands of kagome metals; this is to represent the flat bands in terms of compact molecular orbitals and describe the system [27–29] in terms of topological Kondo lattice models [30, 31]. Importantly, as dictated by band topology, the compact molecular orbitals must hybridize with other orbitals. The competition between this hybridization and the tendency of the active flat bands to form static electronic order leads to a quantum critical regime where Landau quasiparticles are lost; the qualitative physics, by analogy with the heavy fermion physics [32] and supported by our calculations reported here, is captured by a schematic phase diagram [see below, Fig. 4 (a)]. We show that the quantum critical fluctuations nucleate a superconducting state that envelopes the corresponding putative quantum critical point (QCP).

We consider the continuum model for twisted bilayer WSe<sub>2</sub>, which describes the low-energy physics. The precise form of band topology is sensitive to parameters such

\* fx7@rice.edu

† jennifer.cano@stonybrook.edu

‡ qmsi@rice.edu

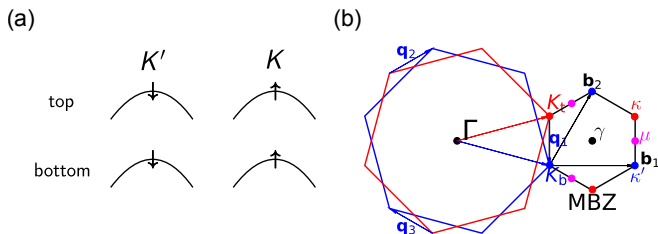


FIG. 1. (a) The spin-valley locking mechanism of transition metal dichalcogenides in the  $2H$  structural phase. (b) The moiré Brillouin zone (black hexagon) is spanned by the difference between the  $K$  (or  $K'$ ) points in the top and bottom layers.

as the strength of the moiré potentials. For definiteness, we focus on the case when the electronic states within the active band subspace arise from a pair of topological flat and dispersive bands with opposite Chern numbers (for each valley), which appears for relatively small twist angles [25]; a similar case arises for larger twist angles, as illustrated in Appendix B. In this case, we are able to construct two molecular orbitals for a real space description, for which the band topology dictates that they hybridize with each other. The Coulomb interactions are described in terms of the molecular orbitals. We study the model in terms of the extended-dynamical mean field theory (EDMFT) method because it is essential to treat the aforementioned competition in a dynamical way (instead of by the Hartree-Fock method) [33], and we use its cluster form so that unconventional pairing can be treated [34].

*Model and method: Band structure and Wannier functions* We start from the low-energy effective model of twisted bilayer  $\text{WSe}_2$  in the  $2H$  structural phase. The single-layer band structure around  $K$  and  $K'$  points in these TMDC materials can be approximately described by a hole pocket with quadratic dispersion. The two hole pockets around the two valleys have opposite spin orientation as shown in Fig. 1(a), which is referred to as spin-valley locking [35, 36].

When the two layers of  $\text{WSe}_2$  are stacked together with a small twisting angle  $\theta$ , the single layer Brillouin zones will have a mismatch, and a moiré superlattice will emerge. The moiré Brillouin zone is spanned by the difference between the  $K$  (or  $K'$ ) points in the top and bottom layers, as shown in Fig. 1(b), in which the reciprocal basis vectors of the moiré Brillouin zone is labeled by  $\mathbf{b}_1$  and  $\mathbf{b}_2$ . The length of the reciprocal lattice vectors can be determined by both the twisting angle  $\theta$  and the single layer lattice constant  $a_0$ :  $|\mathbf{b}_{1,2}| = 8\pi \sin(\theta/2)/\sqrt{3}a_0$ . Accordingly, the Bravais lattice basis vectors of this moiré superlattice can be determined by  $\mathbf{a}_i \cdot \mathbf{b}_j = 2\pi\delta_{ij}$ .

The continuum Hamiltonian, which is discussed in detail in Appendix A, can be constructed to compute the band structure of twisted bilayer  $\text{WSe}_2$ . In Fig. 2, we show the band structure of the continuum model with

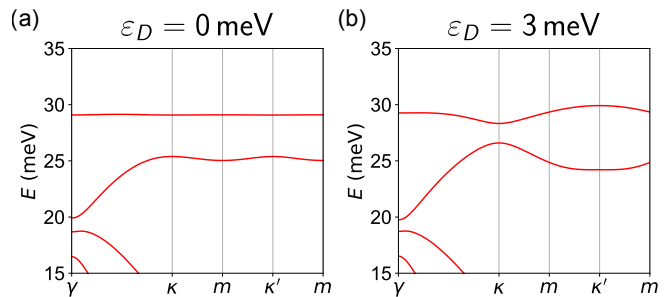


FIG. 2. Single valley band structure of the continuum model with two different displacement field strengths. In both cases, the top two moiré bands carry opposite Chern numbers. The twisting angle is chosen to be  $\theta = 1.43^\circ$  for illustration purpose; similar considerations apply to larger twist angles (Appendix B).

two different displacement field strengths, with the twisting angle  $\theta = 1.43^\circ$ ; a similar regime of band topology can also arise for larger twisting angles as illustrated in Appendix B. The top two bands carry opposition Chern numbers, which allow us to construct two  $C_{3z}$  symmetric moiré orbitals. In both cases, the top-most band has  $C_{3z}$  eigenvalues of  $\omega = e^{i2\pi/3}$ ,  $\omega^*$  and  $\omega^*$  at  $\gamma$ ,  $\kappa$  and  $\kappa'$  points, respectively. While the second band has  $C_{3z}$  eigenvalues of  $\omega, 1, 1$  at these three points. These symmetry eigenvalues are compatible with the summation of two  ${}^2E$  orbitals at the  $1b$  [ $\tau_1 = (2\mathbf{a}_1 + \mathbf{a}_2)/3$ ] and  $1c$  [ $\tau_2 = (\mathbf{a}_1 + 2\mathbf{a}_2)/3$ ] Wyckoff positions of the space group  $P3$  [37].

Using WANNIER90 [38] program, we are able to obtain a two-orbital tight-binding model, which faithfully describe the two active bands of the continuum model. The projection of the two moiré orbitals onto the top bands are shown in Figs. 3(a-b), in which the displacement field strength is chosen to be  $\varepsilon_D = 3 \text{ meV}$ . The Wannier functions of the two moiré orbitals are shown in Fig. 3(c), in which the two orbitals are localized at the  $1b$  and  $1c$  Wyckoff positions.

Consequently, a single valley two-orbital model can be obtained:

$$H_{\text{TB}}^K = \sum_{\mathbf{R}_0 \mathbf{R} \alpha \beta} t_{\alpha\beta}(\mathbf{R}) c_{\mathbf{R}+\mathbf{R}_0, \alpha, \uparrow}^\dagger c_{\mathbf{R}_0, \beta, \uparrow}. \quad (1)$$

The values of some of the hopping parameters with short hopping distance are listed in Table I in Appendix C. Since the two valleys (spins) are related by time-reversal symmetry, the tight-binding parameters for the  $K'$  valley are complex conjugate of those for the  $K$  valley:

$$H_{\text{TB}}^{K'} = \sum_{\mathbf{R}_0 \mathbf{R} \alpha \beta} t_{\alpha\beta}^*(\mathbf{R}) c_{\mathbf{R}+\mathbf{R}_0, \alpha, \downarrow}^\dagger c_{\mathbf{R}_0, \beta, \downarrow}. \quad (2)$$

The weak displacement field breaks the  $C_{2y}T$  symmetry, and the two orbitals contribute to the two active bands with different intensities. As shown in Fig. 3(d),

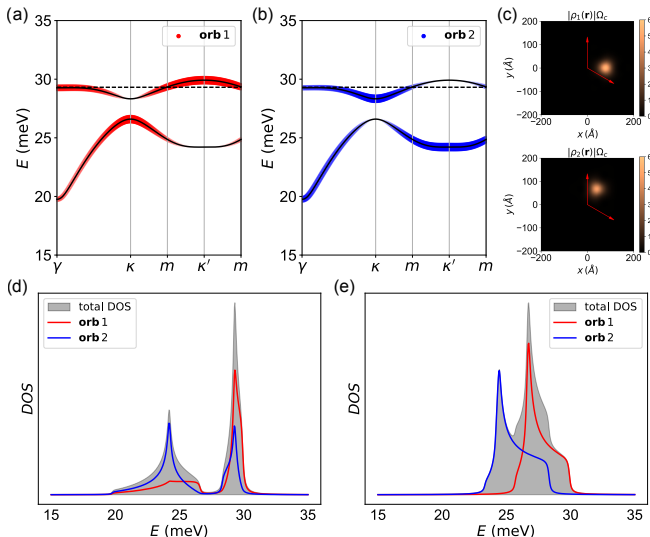


FIG. 3. (a-b) The fat band projection of the two moiré orbitals with displacement field potential strength  $\epsilon_D = 3$  meV. The dashed lines stand for the Fermi level in the non-interacting band structure at hole filling factor  $\nu = 1$ . (c) The density distribution of the Wannier functions of the two moiré orbitals. The two red arrows stand for the Bravais lattice basis vectors. (d) The density of states of the two-orbital tight-binding model. (e) The density of states with the hybridization between the two orbitals removed.

the first orbital at  $1b$  Wyckoff position has a larger weight in the top band, while the second orbital at  $1c$  Wyckoff position has a larger weight in the second band. As already emphasized, the topological nature of the bands ensure that the two orbitals hybridize with each other. In fact, the nearest-neighbor hybridization between the two orbitals is noticeably larger than the intra-orbital hopping terms. When these hybridization terms are turned off, *i.e.*,  $t_{\alpha\beta}(\mathbf{R})$  are set to 0 when  $\alpha \neq \beta$ , the gap between the two bands will vanish, as shown in Fig. 3(e). In this case, the density of states distribution of the two orbitals are noticeably separated due to the on-site potential difference. As a result, the relative fillings of these two orbitals at total hole filling  $\nu = 1$  will be different, leading to orbital-selective correlations, with those closer to half-filling experiencing stronger correlation effects [19].

*Model and method: Interaction Hamiltonian* With the two-orbital tight-binding model at hand, we can now construct the interaction Hamiltonian. The direct channel of the interaction elements in the Wannier basis can be written in the following form:

$$U_{\alpha\beta}(\mathbf{R}) = \frac{1}{2} \int d^2r d^2r' U(\mathbf{r} - \mathbf{r}') |W_\alpha(\mathbf{r} - \mathbf{R})|^2 |W_\beta(\mathbf{r}')|^2, \quad (3)$$

in which  $U(\mathbf{r})$  is the double-gate screened Coulomb interaction, and  $W_\alpha(\mathbf{r})$  stands for the Wannier functions of the moiré orbitals. The expression of the screened

Coulomb interaction is given by:

$$U(\mathbf{r}) = \frac{e^2}{4\pi\epsilon_0\epsilon d} \sum_{n=-\infty}^{+\infty} \frac{1}{\sqrt{n^2 + (r/d)^2}}. \quad (4)$$

Here  $d = 100\text{\AA}$  is the gate distance and  $\epsilon$  is the dielectric constant of the material. Numerically performing the integral in Eq. (3), we conclude that the on-site interaction  $U$  is on the order of magnitude of  $10 \sim 35$  meV, assuming the dielectric constant is around  $10 \sim 30$ . In addition, due to the slightly smaller size of the  $1b$  moiré orbital, the on-site interaction  $U_{1b}$  is slightly larger than  $U_{1c}$ . Besides, we also find that the nearest-neighbor interaction is smaller than 20% of the on-site interaction  $U$ , and all exchange interactions are smaller than 5% of  $U$ , so the Hubbard terms are dominant [39]. As a consequence, the effective interaction Hamiltonian can be written as:

$$H_I = U \sum_{\mathbf{R}_0\alpha} n_{\mathbf{R}_0,\alpha,\uparrow} n_{\mathbf{R}_0,\alpha,\downarrow}. \quad (5)$$

*Model and method: Extended-dynamical mean field theory* In practice, orbital 1 has a hole occupancy ( $\approx 0.8$ ) that is considerably closer to half-filling than orbital 2 (which has a hole occupancy  $\approx 0.2$ ) in the non-interacting band structure. In the following, we will denote orbitals 1 and 2 as the more localized  $f$  and conduction electron  $c$  orbitals, respectively, and focus our treatment on the correlation effects of the  $f$  orbital. This leads to an effective periodic Anderson Hamiltonian, which takes the form:

$$H_{\text{AL}} = \sum_{\mathbf{p},\sigma} (\epsilon_{\mathbf{p}} - \mu) c_{\mathbf{p}\sigma}^\dagger c_{\mathbf{p}\sigma} + \sum_i [(\epsilon_f - \mu) n_{fi} + U n_{fi\uparrow} n_{fi\downarrow}] + \sum_{\mathbf{p},i\sigma} (V_{\mathbf{p}i} c_{\mathbf{p}\sigma}^\dagger f_{i\sigma} + \text{h.c.}) + \sum_{i,j,m} I_{ij} S_{fi}^m S_{fj}^m, \quad (6)$$

where  $c_{\mathbf{p}\sigma}$  ( $f_{i\sigma}$ ) annihilates a  $c$  ( $f$ ) electron at momentum  $\mathbf{p}$  (lattice site  $i$ ) with spin  $\sigma$ ,  $\epsilon_{\mathbf{p}}$  is the dispersion of the conduction electrons while  $\epsilon_f$  and  $U$  denote the  $f$ -level energy and on-site Coulomb repulsion, respectively. In addition,  $\mu$  is the chemical potential. Without loss of generality, we treat the hybridization between the  $f$  and  $c$  electrons at an average level, setting  $V_{\mathbf{p}i} = V$ .  $I_{ij}$  represents the emergent RKKY exchange interactions, mediated by the conduction  $c$  electrons, for the Cartesian component  $m \in \{x, y, z\}$  of the  $f$  electrons. We use the following estimated parameters:  $\epsilon_f = 27.60$  meV,  $U = 10$  meV,  $V = 2.5$  meV, and  $\mu = 27.67$  meV. Additionally, for the self-consistent calculation we would need the input for a bare conduction electron density of states, which describes  $\epsilon_{\mathbf{p}}$  and is given by the blue curve in Fig. 3(e). Varying the ratio of  $I_{ij}$  to  $T_K^0$ , the bare Kondo energy scale, tunes the system across metallic quantum criticality.

We study the effective model described above using the EDMFT method [33]. To facilitate the investigation of unconventional superconducting pairing, we uti-

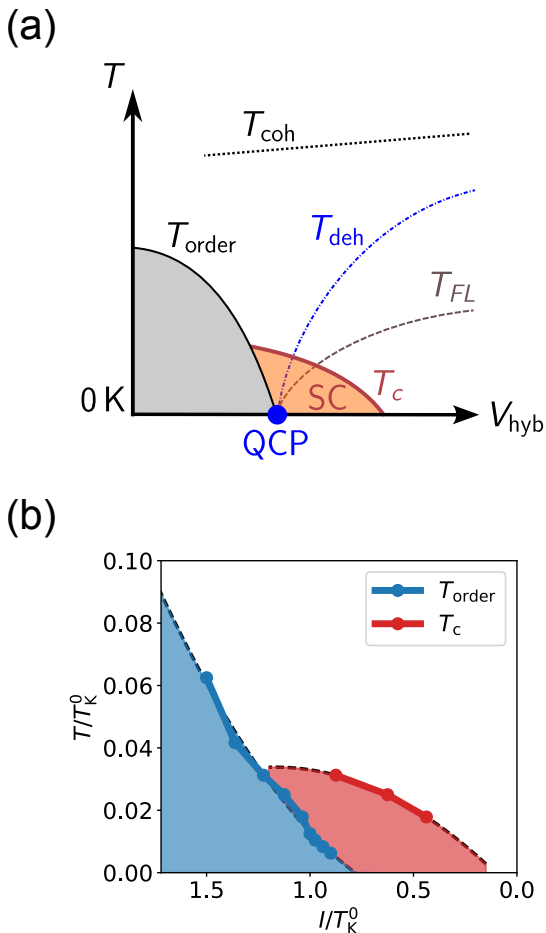


FIG. 4. (a) Schematic phase diagram in temperature and as a function of the hybridization strength,  $V_{\text{hyb}}$ , for a fixed set of interaction and other coupling parameters. It shows the vanishing of the dehybridization energy scale ( $T_{\text{deh}}$ ) [32, 40] at the QCP. Here  $T_{\text{order}}$  and  $T_c$  are the transition temperatures to an electronic order and to superconducting state (SC), respectively.  $T_{\text{FL}}$  is a low-temperature crossover scale into a Fermi liquid, and  $T_{\text{coh}}$  a high-temperature crossover scale for the initial onset of Kondo coherence. (b) Finite-temperature phase diagram as a function of the control parameter  $I/T_K^0$  (which is tuned by the hybridization) obtained from C-EDMFT calculations, with  $T_c$  and  $T_{\text{order}}$  marked by red and blue circles, respectively.

lize a cluster version of the EDMFT (C-EDMFT) approach [34], which determines correlation functions of  $H_{\text{AL}}$  in terms of a self-consistently determined two-site quantum cluster model that involves both fermionic and bosonic baths. The numerically exact continuous-time Monte Carlo method is used to solve the effective cluster model at nonzero temperatures.

*Quantum fluctuations and superconductivity* Our mapping establishes the connection between tWSe<sub>2</sub> and canonical heavy fermion systems, where quantum fluctuations have been proven to play a crucial role, giving rise

to such phenomena as metallic quantum criticality and unconventional superconductivity [34].

Our results are shown in Fig. 4(b). Because the chemical potential passes through the flat band [*c.f.* Fig. 3(a)], the development of an electronic order is natural. The hybridization promotes the Kondo effect; increasing it amounts to decreasing the ratio  $I/T_K^0$  [going rightward in Fig. 4(b)]. It weakens the order, eventually suppressing it and reaching a QCP.

The unconventional pairing and superconductivity are primarily driven by the spin-flip component of the RKKY interaction, which plays a crucial role in the formation of spin-singlet Cooper pairs. We calculate the static lattice pairing susceptibility [34], whose divergence identifies the superconducting transition temperature  $T_c$ . We perform these calculations at various temperatures to determine the finite-temperature phase boundary for the superconducting phase. The resulting phase diagram is displayed in Fig. 4(b), with the temperatures measured by the bare Kondo temperature ( $T_K^0$ ), which serves as the effective Fermi temperature. The region of superconducting order is anchored by the underlying QCP. The superconducting transition temperature  $T_c$  near the QCP reaches approximately 3% of the Fermi temperature.

We can further clarify the qualitative physics by drawing analogy to heavy fermion systems. Thus, our numerical results can be understood in terms of an overall phase diagram, which is illustrated in Fig. 4(a). At the QCP, not only does the transition from order to disorder take place, but a new energy scale,  $T_{\text{deh}}$ —which characterizes the hybridization-dehybridization between the  $f$  and  $c$  electrons—also vanishes [13, 32, 40–42], indicating a critical destruction of Landau quasiparticles. The superconducting phase emerges near the QCP, where the quantum fluctuations are the most pronounced.

*Discussion and summary* Several remarks are in order. Firstly, for the correlated phase we have emphasized the electronic order. At commensurate filling, this phase is naturally insulating like, as is observed experimentally [15]. In contrast, away from commensurate filling, the system would stay metallic, which also is seen experimentally [16].

Secondly, our work highlights the role of quantum fluctuations. While such fluctuations are the most pronounced in the quantum critical regime (*cf.* Fig. 4(a)), their influence operates over a much wider range. Experimentally, the  $T^2$  resistivity  $A$  coefficient is found to increase by an order of magnitude as the tWSe<sub>2</sub> system is tuned (by carrier concentration) [15] towards the superconducting regime, which is a canonical indication for the influence of the type of quantum criticality that loses quasiparticles [32, 41]. We note in passing that related Kondo lattice behavior in hetero-layers of TMDCs has been observed experimentally [43, 44] and discussed theoretically [45, 46]. We also note on proposed mechanisms for superconductivity in the tWSe<sub>2</sub> system from spin liquid behavior or Luttinger-Kohn mechanism near van-Hove singularity and, thus, unrelated to quantum

criticality [47, 48].

Thirdly, our work reveals a description of the tWSe<sub>2</sub> system in terms of a topological Kondo lattice. This is expected to give rise to Kondo like behavior in the temperature dependence of the electrical resistivity, which can be most clearly captured in the regime near the coherence temperature. Such behavior is indeed seen experimentally [15]. At the same time, in the absence of the displacement field, the  $C_{2y}T$  symmetry would render the Kondo lattice to a two-orbital extended Hubbard model. We expect a smooth crossover of the physics between the two regimes.

Finally, our results capture the high superconducting transition temperature in the sense that  $T_c$  is about a few percent of the Fermi temperature. This feature is shared by such bulk correlated materials as the heavy fermion metals and cuprates [32, 34]. The mechanism advanced here reflects the quantum fluctuations enabled by electronic topology at intermediate correlations, and this is very different from how quantum fluctuations develop in canonical heavy fermion metals and in the cuprates. On the other hand, our results suggest that  $T_c$  measured by the Fermi temperature is nearly universal regardless of the precise origin of the quantum fluctuations that drive the superconductivity. As such, our work reveals new connections between the unconventional superconductivity across the platforms for strongly correlated systems. This interconnection suggests that the mechanism we have advanced may operate in other correlated systems, including other moiré structures [49–52] and kagome and pyrochlore systems [27–29, 53] that connect with heavy fermions.

To summarize, we have advanced a mechanism for superconductivity recently discovered in the twisted WSe<sub>2</sub> moiré structures. We show how the electronic topology in this system enables quantum fluctuations, which gives rise to quantum criticality and the concomitant superconductivity. More generally, our results suggest that, in suitable regimes of correlations, band topology amounts to quantum fluctuations. Furthermore, our work reveals new connections among a variety of strongly correlated systems.

## ACKNOWLEDGMENTS

We thank Valentin Crépel, Zhongdong Han, Andrew Millis, Abhay Pasupathy, Silke Paschen, Yiyu Xia and Yonglong Xie and, particularly Kin Fai Mak and Jie Shan for useful discussions. This work has been supported in part by the NSF Grant No. DMR-2220603 (F.X. and L.C.), the AFOSR under Grant No. FA9550-21-1-0356 (S.S., Y.F.), the Robert A. Welch Foundation Grant No. C-1411 (Q.S.) and the Vannevar Bush Faculty Fellowship ONR-VB N00014-23-1-2870 (Q.S.). J.C. acknowledges the support of the National Science Foundation under Grant No. DMR-1942447, support from the Alfred P. Sloan Foundation through a Sloan Research Fel-

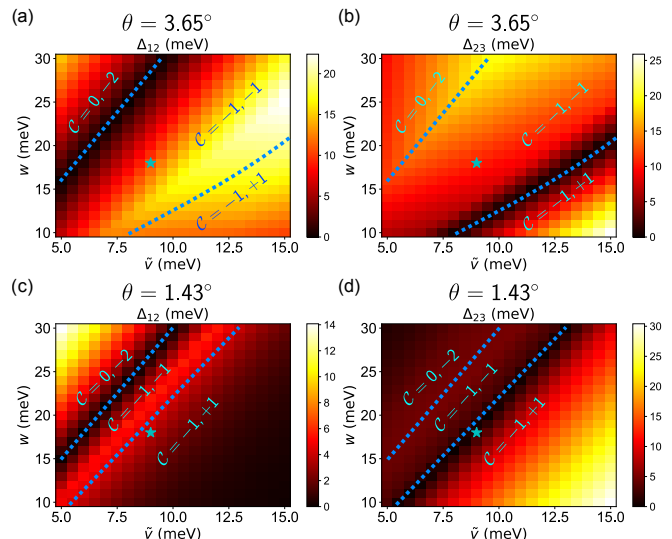


FIG. 5. (a-b) The smallest direct band gap between the first and second top-most bands ( $\Delta_{12}$ ), and between the second and the third top-most bands ( $\Delta_{23}$ ) as functions of the moiré potential strength  $\tilde{v}$  and  $w$ , with twisting angle  $\theta = 3.65^\circ$ . (c-d) The smallest direct band gaps with twisting angle  $\theta = 1.43^\circ$ . The parameters used in Ref. [25] are labeled by the cyan star. The dashed lines indicate topological phase transitions, with the Chern numbers of the top two bands labeled. Here we set the displacement field potential strength to be  $\varepsilon_D = 0$  meV, and  $\psi = 128^\circ$ .

lowship and the support of the Flatiron Institute, a division of the Simons Foundation. The majority of the computational calculations have been performed on the Shared University Grid at Rice funded by NSF under Grant No. EIA-0216467, a partnership between Rice University, Sun Microsystems, and Sigma Solutions, Inc., the Big-Data Private-Cloud Research Cyberinfrastructure MRI-award funded by NSF under Grant No. CNS-1338099, and the Extreme Science and Engineering Discovery Environment (XSEDE) by NSF under Grant No. DMR170109. Q.S. acknowledges the hospitality of the Aspen Center for Physics, which is supported by NSF grant No. PHY-2210452.

## Appendix A: Continuum model

In this appendix, we provide a brief discussion about the continuum model of twisted homo-bilayer TMDC, which was introduced in Ref. [24]. With the inter-layer and intra-layer moiré potential considered, the low-energy effective Hamiltonian of twisted bilayer WSe<sub>2</sub> can be written as:

$$H = \begin{pmatrix} \frac{\nabla^2}{2m^*} + v_+(\mathbf{r}) + \frac{\varepsilon_D}{2} & t(\mathbf{r}) \\ t^*(\mathbf{r}) & \frac{\nabla^2}{2m^*} + v_-(\mathbf{r}) - \frac{\varepsilon_D}{2} \end{pmatrix}. \quad (\text{A1})$$

#	$\alpha$	$\beta$	$R_1$	$R_2$	$ t_{\alpha\beta}(\mathbf{R}) $ (meV)	$\arg t_{\alpha\beta}(\mathbf{R})$
1	1	1	0	0	27.60	$0.0^\circ$
2	2	2	0	0	25.63	$0.0^\circ$
3	2	1	0	-1	1.39	$36.5^\circ$
4	1	2	0	1	1.39	$-36.5^\circ$
5	1	2	-1	0	1.39	$-36.5^\circ$
6	2	1	0	0	1.39	$36.5^\circ$
7	1	2	0	0	1.39	$-36.5^\circ$
8	2	1	1	0	1.39	$36.5^\circ$
9	2	2	-1	-1	0.52	$-121.9^\circ$
10	2	2	-1	0	0.52	$121.9^\circ$
11	2	2	0	-1	0.52	$121.9^\circ$
12	2	2	0	1	0.52	$-121.9^\circ$
13	2	2	1	0	0.52	$-121.9^\circ$
14	2	2	1	1	0.52	$121.9^\circ$
15	1	1	-1	-1	0.43	$125.3^\circ$
16	1	1	-1	0	0.43	$-125.3^\circ$
17	1	1	0	-1	0.43	$-125.3^\circ$
18	1	1	0	1	0.43	$125.3^\circ$
19	1	1	1	0	0.43	$125.3^\circ$
20	1	1	1	1	0.43	$-125.3^\circ$
21	2	1	-1	-1	0.16	$-143.5^\circ$
22	1	2	-1	-1	0.16	$143.5^\circ$
23	1	2	-1	1	0.16	$143.5^\circ$
24	2	1	1	-1	0.16	$-143.5^\circ$
25	2	1	1	1	0.16	$-143.5^\circ$
26	1	2	1	1	0.16	$143.5^\circ$
27	1	2	-2	0	0.12	$-38.1^\circ$
28	2	1	-1	-2	0.12	$38.1^\circ$
29	1	2	0	-1	0.12	$-38.1^\circ$
30	2	1	0	1	0.12	$38.1^\circ$
31	1	2	1	2	0.12	$-38.1^\circ$
32	2	1	2	0	0.12	$38.1^\circ$
33	1	2	-2	-1	0.12	$-34.9^\circ$
34	2	1	-1	0	0.12	$34.9^\circ$
35	2	1	0	-2	0.12	$34.9^\circ$
36	1	2	0	2	0.12	$-34.9^\circ$
37	1	2	1	0	0.12	$-34.9^\circ$
38	2	1	2	1	0.12	$34.9^\circ$

TABLE I. Parameters of the single valley tight-binding model with  $\theta = 1.43^\circ$  and  $\varepsilon_D = 3$  meV. The variables  $R_1, R_2 \in \mathbb{Z}$  stand for the components of the hopping vector  $\mathbf{R} = R_1\mathbf{a}_1 + R_2\mathbf{a}_2$ . Note that the first two rows are the on-site energies of the two orbitals.

in which  $m^*$  is the effective mass of the hole pocket,  $v_\pm(\mathbf{r})$  is the moiré potential in the top and bottom layers, respectively, and  $t(\mathbf{r})$  is the inter-layer tunneling term. The displacement field potential  $\varepsilon_D$  is also considered in the Hamiltonian. In the absence of the displacement field, the Hamiltonian Eq. (A1) possess both  $C_{3z}$  and  $C_{2y}T$  symmetries, while the displacement field will break the  $C_{2y}T$  symmetry. Under the lowest-harmonic approx-

imation [24], the  $C_{3z}$  symmetry enforces the intra-layer periodic potential to have the following form:

$$v_\ell(\mathbf{r}) = 2\tilde{v} \sum_{j=1,3,5} \cos(\mathbf{g}_j \cdot \mathbf{r} + \ell\psi), \quad \ell = \pm, \quad (\text{A2})$$

in which the reciprocal lattice vectors are defined as  $\mathbf{g}_1 = -\mathbf{g}_4 = \mathbf{b}_1$ ,  $\mathbf{g}_3 = -\mathbf{g}_6 = \mathbf{b}_2 - \mathbf{b}_1$  and  $\mathbf{g}_5 = -\mathbf{g}_2 = -\mathbf{b}_2$ . Similarly, the inter-layer tunneling term can be written as:

$$t(\mathbf{r}) = w \sum_{j=1,2,3} e^{i\mathbf{q}_j \cdot \mathbf{r}}, \quad (\text{A3})$$

in which the definition of the three  $\mathbf{q}_j$  vectors can be found in Fig. 1(b). By fitting the continuum Hamiltonian Eq. (A1) with *ab initio* simulations, the parameters for twisted bilayer WSe<sub>2</sub> are determined to be  $a_0 = 3.317$  Å,  $m^* = 0.43m_e$ ,  $\tilde{v} = 9$  meV,  $\psi = 128^\circ$  and  $w = 18$  meV, in which  $m_e$  is the mass of the free electron [25]. Band structure shown in Fig. 2 is computed from this continuum model.

## Appendix B: Band topology

In this appendix, we will discuss the band structure and the associated band topology of twisted bilayer WSe<sub>2</sub> with different moiré potential strengths. As indicated by the continuum model Hamiltonian in Eq. (A1), the band structure is mostly determined by the twisting angle  $\theta$  and the moiré potential strength  $\tilde{v}$  and  $w$ , and is expected to be sensitive to such parameters [54].

Here, we study the band structure and the topology of the top bands in the case of tWSe<sub>2</sub> with the angle  $\psi = 128^\circ$  and effective mass  $m^* = 0.43m_e$  fixed. In Fig. 5, we show the direct band gaps between the first and the second top-most bands  $\Delta_{12}$ , and between the second and the third top-most bands  $\Delta_{23}$  as functions of the moiré potential strength  $\tilde{v}$  and  $w$ , with the twisting angles  $\theta = 3.65^\circ$  and  $\theta = 1.43^\circ$ . We vary the strength of the intra-layer potential  $\tilde{v}$  from 5 to 15 meV, and the inter-layer potential  $w$  from 10 to 30 meV. It can be seen that with a moderate change of the moiré potential strength, it is possible to obtain a band structure with the top two bands carrying zero total Chern number, even if the twisting angle is  $\theta = 3.65^\circ$ .

## Appendix C: Tight-binding parameters

The values of the hopping parameters for the two-orbital tight-binding model, which are greater than 0.1 meV, with parameters  $\theta = 1.43^\circ$  and  $\varepsilon_D = 3$  meV, are listed in Table I.

- 
- [1] Y. Cao, V. Fatemi, A. Demir, S. Fang, S. L. Tomarken, J. Y. Luo, J. D. Sanchez-Yamagishi, K. Watanabe, T. Taniguchi, E. Kaxiras, *et al.*, *Nature* **556**, 80 (2018).
- [2] Y. Cao, V. Fatemi, S. Fang, K. Watanabe, T. Taniguchi, E. Kaxiras, and P. Jarillo-Herrero, *Nature* **556**, 43 (2018).
- [3] E. C. Regan, D. Wang, C. Jin, M. I. Bakti Utama, B. Gao, X. Wei, S. Zhao, W. Zhao, Z. Zhang, K. Yumigeta, *et al.*, *Nature* **579**, 359 (2020).
- [4] Y. Tang, L. Li, T. Li, Y. Xu, S. Liu, K. Barmak, K. Watanabe, T. Taniguchi, A. H. MacDonald, J. Shan, *et al.*, *Nature* **579**, 353 (2020).
- [5] L. Wang, E.-M. Shih, A. Ghiotto, L. Xian, D. A. Rhodes, C. Tan, M. Claassen, D. M. Kennes, Y. Bai, B. Kim, *et al.*, *Nature materials* **19**, 861 (2020).
- [6] Y. Xu, S. Liu, D. A. Rhodes, K. Watanabe, T. Taniguchi, J. Hone, V. Elser, K. F. Mak, and J. Shan, *Nature* **587**, 214 (2020).
- [7] T. Li, S. Jiang, B. Shen, Y. Zhang, L. Li, Z. Tao, T. Devakul, K. Watanabe, T. Taniguchi, L. Fu, *et al.*, *Nature* **600**, 641 (2021).
- [8] J. Cai, E. Anderson, C. Wang, X. Zhang, X. Liu, W. Holtzmann, Y. Zhang, F. Fan, T. Taniguchi, K. Watanabe, *et al.*, *Nature* **622**, 63 (2023).
- [9] Y. Zeng, Z. Xia, K. Kang, J. Zhu, P. Knüppel, C. Vaswani, K. Watanabe, T. Taniguchi, K. F. Mak, and J. Shan, *Nature* **622**, 69 (2023).
- [10] H. Park, J. Cai, E. Anderson, Y. Zhang, J. Zhu, X. Liu, C. Wang, W. Holtzmann, C. Hu, Z. Liu, *et al.*, *Nature* **622**, 74 (2023).
- [11] F. Xu, Z. Sun, T. Jia, C. Liu, C. Xu, C. Li, Y. Gu, K. Watanabe, T. Taniguchi, B. Tong, J. Jia, Z. Shi, S. Jiang, Y. Zhang, X. Liu, and T. Li, *Phys. Rev. X* **13**, 031037 (2023).
- [12] B. Keimer and J. E. Moore, *Nature Physics* **13**, 1045 (2017).
- [13] S. Paschen and Q. Si, *Nat. Rev. Phys.* **3**, 9 (2021).
- [14] E. Y. Andrei and A. H. MacDonald, *Nature materials* **19**, 1265 (2020).
- [15] Y. Xia, Z. Han, K. Watanabe, T. Taniguchi, J. Shan, and K. F. Mak, *arXiv e-prints*, arXiv:2405.14784 (2024), arXiv:2405.14784 [cond-mat.mes-hall].
- [16] Y. Guo, J. Pack, J. Swann, L. Holtzman, M. Cothrine, K. Watanabe, T. Taniguchi, D. Mandrus, K. Barmak, J. Hone, A. J. Millis, A. N. Pasupathy, and C. R. Dean, *arXiv e-prints*, arXiv:2406.03418 (2024), arXiv:2406.03418 [cond-mat.mes-hall].
- [17] P. A. Lee, N. Nagaosa, and X.-G. Wen, *Rev. Mod. Phys.* **78**, 17 (2006).
- [18] Q. Si and F. Steglich, *Science* **329**, 1161 (2010).
- [19] Q. Si, R. Yu, and E. Abrahams, *Nature Reviews Materials* **1**, 16017 (2016).
- [20] F. Wu, A. H. MacDonald, and I. Martin, *Phys. Rev. Lett.* **121**, 257001 (2018).
- [21] H. Isobe, N. F. Q. Yuan, and L. Fu, *Phys. Rev. X* **8**, 041041 (2018).
- [22] H. Guo, X. Zhu, S. Feng, and R. T. Scalettar, *Phys. Rev. B* **97**, 235453 (2018).
- [23] C. Xu and L. Balents, *Physical review letters* **121**, 087001 (2018).
- [24] F. Wu, T. Lovorn, E. Tutuc, I. Martin, and A. H. MacDonald, *Phys. Rev. Lett.* **122**, 086402 (2019).
- [25] T. Devakul, V. Crépel, Y. Zhang, and L. Fu, *Nature Communications* **12**, 6730 (2021).
- [26] A. P. Reddy, F. Alsallom, Y. Zhang, T. Devakul, and L. Fu, *Phys. Rev. B* **108**, 085117 (2023).
- [27] H. Hu and Q. Si, *Science Advances* **9**, eadg0028 (2023).
- [28] L. Chen, F. Xie, S. Sur, H. Hu, S. Paschen, J. Cano, and Q. Si, *Nature Communications* **15**, 5242 (2024).
- [29] L. Chen, F. Xie, S. Sur, H. Hu, S. Paschen, J. Cano, and Q. Si, *arXiv e-prints*, arXiv:2307.09431 (2023), arXiv:2307.09431 [cond-mat.str-el].
- [30] H.-H. Lai, S. E. Grefe, S. Paschen, and Q. Si, *Proceedings of the National Academy of Sciences* **115**, 93 (2018).
- [31] S. Dzsaber, X. Yan, M. Taupin, G. Eguchi, A. Prokofiev, T. Shiroka, P. Blaha, O. Rubel, S. E. Grefe, H.-H. Lai, *et al.*, *Proceedings of the National Academy of Sciences* **118**, e2013386118 (2021).
- [32] H. Hu, L. Chen, and Q. Si, *arXiv e-prints*, arXiv:2210.14183 (2022), *Nat. Phys.*, to appear, arXiv:2210.14183 [cond-mat.str-el].
- [33] H. Hu, L. Chen, and Q. Si, *arXiv e-prints*, arXiv:2210.14197 (2022), arXiv:2210.14197 [cond-mat.str-el].
- [34] H. Hu, A. Cai, L. Chen, L. Deng, J. H. Pixley, K. Ingersent, and Q. Si, *arXiv e-prints*, arXiv:2109.13224 (2021), arXiv:2109.13224 [cond-mat.str-el].
- [35] G.-B. Liu, W.-Y. Shan, Y. Yao, W. Yao, and D. Xiao, *Phys. Rev. B* **88**, 085433 (2013).
- [36] A. Kormányos, G. Burkard, M. Gmitra, J. Fabian, V. Zolyomi, N. D. Drummond, and V. Fal'ko, *2D Materials* **2**, 022001 (2015).
- [37] B. Bradlyn, L. Elcoro, J. Cano, M. G. Vergniory, Z. Wang, C. Felser, M. I. Aroyo, and B. A. Bernevig, *Nature* **547**, 298 (2017).
- [38] G. Pizzi, V. Vitale, R. Arita, S. Blügel, F. Freimuth, G. Géranton, M. Gibertini, D. Gresch, C. Johnson, T. Koretsune, J. Ibañez-Azpiroz, H. Lee, J.-M. Lihm, D. Marchand, A. Marrazzo, Y. Mokrousov, J. I. Mustafa, Y. Nohara, Y. Nomura, L. Paulatto, S. Poncé, T. Ponweiser, J. Qiao, F. Thöle, S. S. Tsirkin, M. Wierzbowska, N. Marzari, D. Vanderbilt, I. Souza, A. A. Mostofi, and J. R. Yates, *Journal of Physics: Condensed Matter* **32**, 165902 (2020).
- [39] F. Wu, T. Lovorn, E. Tutuc, and A. H. MacDonald, *Phys. Rev. Lett.* **121**, 026402 (2018).
- [40] Q. Si, S. Rabello, K. Ingersent, and J. Smith, *Nature* **413**, 804 (2001).
- [41] S. Kirchner, S. Paschen, Q. Chen, S. Wirth, D. Feng, J. D. Thompson, and Q. Si, *Rev. Mod. Phys.* **92**, 011002 (2020).
- [42] S. Paschen, T. Lühmann, S. Wirth, P. Gegenwart, O. Trovarelli, C. Geibel, F. Steglich, P. Coleman, and Q. Si, *Nature* **432**, 881 (2004).
- [43] W. Zhao, B. Shen, Z. Tao, Z. Han, K. Kang, K. Watanabe, T. Taniguchi, K. F. Mak, and J. Shan, *Nature* **616**, 61 (2023).
- [44] W. Zhao, B. Shen, Z. Tao, S. Kim, P. Knüppel, Z. Han, Y. Zhang, K. Watanabe, T. Taniguchi, D. Chowdhury, J. Shan, and K. F. Mak, *arXiv e-prints*, arXiv:2310.06044 (2023), arXiv:2310.06044 [cond-mat.str-el].

- [45] D. Guerci, J. Wang, J. Zang, J. Cano, J. H. Pixley, and A. Millis, *Science Advances* **9**, eade7701 (2023).
- [46] F. Xie, L. Chen, and Q. Si, *Phys. Rev. Res.* **6**, 013219 (2024).
- [47] S. Kim, J. F. Mendez-Valderrama, X. Wang, and D. Chowdhury, *arXiv e-prints*, arXiv:2406.03525 (2024), arXiv:2406.03525 [cond-mat.str-el].
- [48] C. Schrade and L. Fu, *arXiv e-prints*, arXiv:2110.10172 (2021), arXiv:2110.10172 [cond-mat.supr-con].
- [49] A. Ramires and J. L. Lado, *Phys. Rev. Lett.* **127**, 026401 (2021).
- [50] Z.-D. Song and B. A. Bernevig, *Phys. Rev. Lett.* **129**, 047601 (2022).
- [51] A. Kumar, N. C. Hu, A. H. MacDonald, and A. C. Potter, *Phys. Rev. B* **106**, L041116 (2022).
- [52] A. Datta, M. J. Calderón, A. Camjayi, and E. Bascones, *Nature Communications* **14**, 5036 (2023).
- [53] J. Huang, L. Chen, Y. Huang, C. Setty, B. Gao, Y. Shi, Z. Liu, Y. Zhang, T. Yilmaz, E. Vescovo, M. Hashimoto, D. Lu, B. I. Yakobson, P. Dai, J.-H. Chu, Q. Si, and M. Yi, *Nat. Phys.* **20**, 603 (2024).
- [54] J. Yu, J. Herzog-Arbeitman, M. Wang, O. Vafek, B. A. Bernevig, and N. Regnault, *Phys. Rev. B* **109**, 045147 (2024).